

Article

Growth and Thermal Conductivity Study of CuCr_2Se_4 - CuCrSe_2 Hetero-Composite Crystals

Haomin Lu ^{1,2,†}, Chenghao Yin ^{2,3,†}, Ruonan Zhan ^{1,2}, Yanyan Zhang ^{1,2}, Yangyang Lv ^{2,3}, Minghui Lu ^{1,2}, Jian Zhou ^{1,2}, Shuhua Yao ^{1,2,*} and Yanbin Chen ^{2,3,*}

¹ Jiangsu Key Laboratory of Artificial Functional Materials, Department of Materials Science and Engineering, Nanjing University, Nanjing 210093, China; mg1934022@smail.nju.edu.cn (H.L.); mf1934070@smail.nju.edu.cn (R.Z.); mf1834078@smail.nju.edu.cn (Y.Z.); luminghui@nju.edu.cn (M.L.); zhoujian@nju.edu.cn (J.Z.)

² National Laboratory of Solid State Microstructures, Nanjing University, Nanjing 210093, China; mg20220052@smail.nju.edu.cn (C.Y.); lvyangws0801@nju.edu.cn (Y.L.)

³ Department of Physics, Nanjing University, Nanjing 210093, China

* Correspondence: shyao@nju.edu.cn (S.Y.); ybchen@nju.edu.cn (Y.C.)

† These authors contributed equally to this work.

Abstract: The CuCrSe_2 shows attractive physical properties, such as thermoelectric and multiferroic properties, but pure-phase CuCrSe_2 crystal is still quite challenging to obtain because CuCr_2Se_4 can be easily precipitated from a CuCrSe_2 matrix. Here, taking the advantage of this precipitation reaction, we grew a series of CuCrSe_2 - CuCr_2Se_4 hetero-composites by adjusting growth parameters and explored their thermal conductivity property. Determined by electron-diffraction, the orientation relationship between these two compounds is $[001] (100) \text{CuCrSe}_2 \parallel [111] (220) \text{CuCr}_2\text{Se}_4$. The out-of-plane thermal conductivity κ of these hetero-composites was measured by a time-domain thermo-reflectance method. Fitting experimental κ by the Boltzmann-Callaway model, we verify that interface scattering plays significant role to κ in CuCrSe_2 - CuCr_2Se_4 hetero-composites, while in a CuCrSe_2 -dominated hetero-composite, both interface scattering and anharmonic three-phonon interaction lead to the lowest κ therein. Our results reveal the thermal conductivity evolution in CuCr_2Se_4 - CuCrSe_2 hetero-composites.

Keywords: thermal conductivity; crystal growth; hetero-composites; microstructure



Citation: Lu, H.; Yin, C.; Zhan, R.; Zhang, Y.; Lv, Y.; Lu, M.; Zhou, J.; Yao, S.; Chen, Y. Growth and Thermal Conductivity Study of CuCr_2Se_4 - CuCrSe_2 Hetero-Composite Crystals. *Crystals* **2022**, *12*, 433. <https://doi.org/10.3390/cryst12030433>

Academic Editor: Pavel Lukáč

Received: 20 December 2021

Accepted: 16 March 2022

Published: 21 March 2022

Publisher's Note: MDPI stays neutral with regard to jurisdictional claims in published maps and institutional affiliations.



Copyright: © 2022 by the authors. Licensee MDPI, Basel, Switzerland. This article is an open access article distributed under the terms and conditions of the Creative Commons Attribution (CC BY) license (<https://creativecommons.org/licenses/by/4.0/>).

1. Introduction

Ternary chromium chalcogenides ACrX_2 ($A = \text{Cu, Ag}$; $X = \text{S, Se, Te}$) are attracting enormous attention in recent years because of their rich physical properties, such as ferroelectric [1,2], multiferroic [3–5], and large magnetic-field-induced strain [6]. For example, CuCrSe_2 has good overall thermoelectric performances of the low thermal conductivity, good electronic transport (carrier concentration can reach $1.7 \times 10^{20} \text{ cm}^{-3}$), and high Seebeck coefficient ($100 \mu\text{V} \cdot \text{K}^{-1}$) at room temperature [7–9]. Remarkably, the low thermal conductivity of CuCrSe_2 is attributed to a novel mechanism: superionic liquid-like diffusivity of Cu ions between two non-equivalent tetrahedral sites at high temperature ($\geq 365 \text{ K}$) [10–13].

However, in the ACrX_2 system, the pure-phase CuCrSe_2 crystal is quite difficult to obtain because of its complex phases, which can be seen from the Cu-Cr-Se ternary solid-state phase diagram [14]. Currently, in a Cu-Cr-Se system, it is easy to obtain the single phase CuCr_2Se_4 , but CuCrSe_2 crystals always coexist with the CuCr_2Se_4 spinel phase, which seems to be responsible for the controversially reported electrical-transport/magnetic results [15,16]. In addition, there are triangle lattice and honeycomb lattice at the (001)-plane of CuCrSe_2 and (111)-plane of CuCr_2Se_4 , respectively, which may host the rich magnetic properties in these compounds or their composites [17]. To reveal the intrinsic properties of

CuCrSe_2 , R. Yano et al. [18] had successfully grown pure-phase CuCrX_2 crystals ($X = \text{Se}, \text{Te}$) through a modified chemical-vapor-transport technique (CVT) by using appropriate heat treatment. Yan et al. had successfully obtained a single-phase CuCrSe_2 ingot by vacuum annealing [7], but the growing conditions reported in their papers are extremely harsh. In short, impurity phases are hard to eliminate and it is difficult to control their quantities.

Generally speaking, hetero-composites/heterostructures are an effective way to give rise to the novel functionalities unavailable in single-phase crystals [19,20]. For example, SnSe-SnSe_2 heterostructures decrease the thermal conductivity of SnSe dramatically [19]. Therefore, we want to explore the thermal conductivity of $\text{CuCrSe}_2\text{-CuCr}_2\text{Se}_4$ composites.

Here, several hetero-composite $\text{CuCrSe}_2\text{-CuCr}_2\text{Se}_4$ crystals were grown by a CVT using the CrCl_3 transport agent. The weight ratio of coexistence of CuCrSe_2 and CuCr_2Se_4 (hetero-composite) phases can be roughly controlled by growth conditions. The orientation relationship between CuCrSe_2 and CuCr_2Se_4 was determined by electron diffraction. The thermal conductivity of these crystals was measured and analyzed through the Boltzmann-Callaway model to determine the sources of the phonon scattering.

2. Experimental

2.1. Material Synthesis

The single CuCrSe_2 and CuCr_2Se_4 crystals were grown by the chemical vapor transport method using CrCl_3 as a transport agent in an evacuated quartz tube. Before growing single crystals, polycrystalline CuCrSe_2 powders were synthesized by the direct solid-state reaction. Mixtures of high purity Cu (Alfa Aesar 99.999%, Ward Hill, MA, USA), Cr (Alfa Aesar 99.999%, USA), and Se (Alfa Aesar 99.999%, USA) elements with a 1:1:2 atomic ratio were sealed in the evacuated quartz tube. The powder was then heated at $950\text{ }^\circ\text{C}$ for 7 days. Then, the tube was quenched in cold water to obtain the mainly CuCrSe_2 polycrystalline powder with a minor CuCr_2Se_4 impurity (XRD data can be seen in Figure S1). The generation mechanism of CuCr_2Se_4 comes from the decomposition of CuCrSe_2 , which works in both polycrystalline powder and crystal growth. Then polycrystalline CuCrSe_2 powders and 5 mg/mL CrCl_3 powders (Alfa Aesar 99.999%, USA) as the transport agents were loaded into the sealed evacuated quartz tube, and then put into a two-zone furnace to grow the crystals. The high-temperature side was kept at the $960\text{ }^\circ\text{C}$, while the temperature of the low-temperature side of the quartz tube was set as a different temperature ($870\text{ }^\circ\text{C}$, $900\text{ }^\circ\text{C}$, and $930\text{ }^\circ\text{C}$) to obtain different gradients. The growth was achieved by establishing a temperature gradient, and then finally a rapid quenching to room temperature from the different growth temperatures. The schematic of the CVT growth equipment is shown in Figure 1. Finally, the millimeter-sized crystals with metallic luster were obtained successfully for 2 weeks growth.

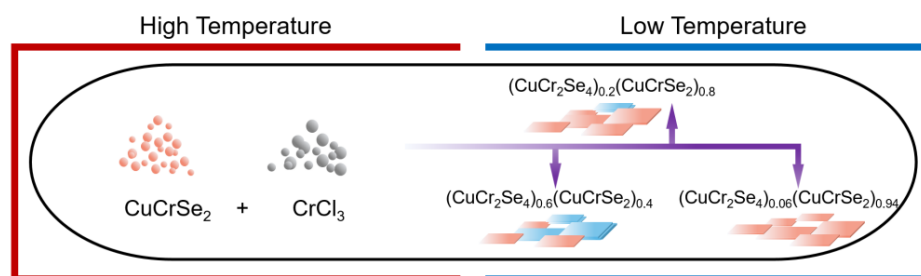


Figure 1. Schematic of the double zone CVT growth furnace and the growth parameters of single $\text{CuCrSe}_2\text{-CuCr}_2\text{Se}_4$ crystals.

2.2. Material Characterization

The crystalline structures were determined by X-ray diffraction (XRD) (Ultima III Rigaku X-ray diffractometer, Cu-K_α radiation, Tokyo, Japan) with 2θ scanned from 10° to 85° . The elemental composition of the as-grown crystals was determined by an energy-dispersive-spectroscopy (EDS) spectrometer equipped in a scanning-electron-microscope

(FEI-Quanta, Hillsboro, OR, USA). The microstructure and crystal structure of the crystals were characterized by a Tecnai F20 transmission electronic microscope (TEM, FEI Inc., Hillsboro, OR, USA). The TEM specimens were prepared by a conventional method including grinding and transferring to a copper grid with carbon coating. The back-reflection Laue detector (MWL120, Multiwire Laboratories, Ltd., Ithaca, NY, USA) was used to determine the crystal structure. The temperature dependences of the thermal conductivities along the *c*-axis were measured by the Time-Domain ThermoReflectance (TDTR) method, which was widely used in the studies of nanoscale thermal transport. Before the TDTR measurement, each sample was polished or cleaved to get a fresh and smooth surface. Each irregular-shaped sample was adhered to the silicon wafer by silver glue for better heat dissipation. Then, a thin layer of aluminum (Al) film with thickness of ~86 nm was deposited on each sample by magnetron sputtering. During the measurements, a train of femtosecond laser pulses (pump beam) arrive on the Al film to heat the surface and serve as the heat source. The surface temperature rises rapidly within several picoseconds, and then declines slowly because of the thermal transport of samples. Meanwhile, a time-delayed femtosecond laser (probe beam) monitors the temperature variation by detecting the temperature-sensitive optical reflectivity. Both the pump and probe laser beams were generated from a mode-locked Ti: sapphire laser (Chameleon, Coherent), and their time delay was precisely controlled by a 600 mm mechanical delay line. The spot diameter of the laser beam was ~20 μm and the thermal penetration depth was ~100 nm, which guaranteed a quasi-one-dimensional heat transport in samples to minimize systematic error caused by the in-plane thermal conductivity [21]. Specifically, the reflected probe signal was received by a silicon-based photodetector, and the in-phase and out-of-phase voltage, i.e., V_{in} and V_{out} , were demodulated by a lock-in amplifier. The thermal conductivities of single crystals were analyzed by fitting the ratio of $-V_{\text{in}}/V_{\text{out}}$ at different delay times using a multilayer thermal transport model [22]. More details of our TDTR technique can be found in our previous works [19,23].

3. Results and Discussion

We show the schematic of the CVT growth equipment, as well as the growth parameters to synthesize the different CuCr_2Se_4 - CuCrSe_2 hetero-composite crystals in Figure 1 (EDS was used to determine the chemical compositions of these samples, see the following Figure 2a). Different CuCrSe_2 - CuCr_2Se_4 hetero-composites can be obtained by rapid quenching from different temperatures. As shown in Figure 1, by quenching at high temperature (~930 °C) we can obtain nearly pure CuCrSe_2 crystals; with a lower quenching temperature (≤ 900 °C), more CuCr_2Se_4 impurity phase can be generated from the matrix of CuCrSe_2 . Using this growth strategy, we grew the different CuCrSe_2 - CuCr_2Se_4 hetero-composites.

Figure 2a displays the EDS spectra of these crystals and we calculated the atomic ratios between CuCrSe_2 and CuCr_2Se_4 phase-in as grown crystals according to quantitative EDS results. The results indicate that the ratios of CuCrSe_2 and CuCr_2Se_4 crystal of three samples are 0.6, 0.8, and 0.94, respectively. Here, as-grown crystals are nominated as $(\text{CuCr}_2\text{Se}_4)_{1-x}(\text{CuCrSe}_2)_x$ ($x = 0.94, 0.8, 0.6$). The optical micrograph of CuCr_2Se_4 - CuCrSe_2 hetero-composite crystals with different composition ratios are shown in the insets of Figure 2a. These crystals show the metallic luster. Figure 2b shows the XRD patterns of as-grown crystal. Evidently, all the reflections of the exposed surface of these samples can be indexed as $(00L)$ - CuCrSe_2 and (LLL) - CuCr_2Se_4 , which suggests the exposed surface of CuCr_2Se_4 crystals being the (111) -plane, while that of CuCrSe_2 crystal is the (001) -plane.

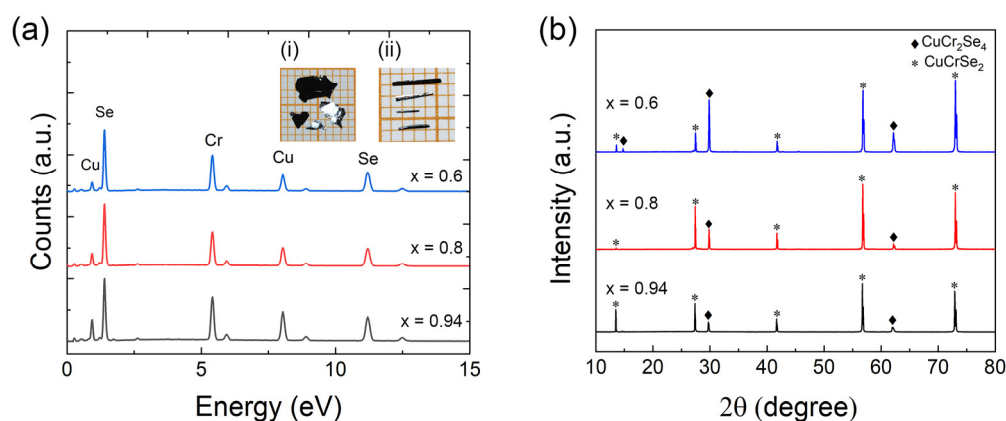


Figure 2. (a) The EDS spectra of $(\text{CuCr}_2\text{Se}_4)_{1-x}(\text{CuCrSe}_2)_x$ ($x = 0.94, 0.8, 0.6$) crystals. The inset of Figure 2a shows the typical photographs of as-grown crystals. (b) The X-ray diffraction patterns of as-grown crystals. Stars and lozenges label the XRD reflections from CuCr_2Se_4 and CuCrSe_2 , respectively.

We also used the TEM to characterize the micro-structure of the $(\text{CuCr}_2\text{Se}_4)_{0.4}(\text{CuCrSe}_2)_{0.6}$ sample. Figure 3 is a typical bright-field TEM image of this sample. Evidently, there are tile structures and Moiré fringes in Figure 3a. Normally, Moiré fringes come from the overlap of two layers with either different structures, or misorientation. The selected-area-electron-diffraction pattern of this area is depicted in Figure 3b. Electron diffraction determination substantiates that there are two sets of diffraction patterns, one is the $[001]\text{-CuCrSe}_2$, and the other is $[111]\text{-CuCr}_2\text{Se}_4$. The in-plane orientation relationship of these two phase is $(2-20)(20-2)\text{-CuCr}_2\text{Se}_4 \parallel (100)(110)\text{-CuCrSe}_2$. To double check the orientation relationship between CuCrSe_2 and CuCr_2Se_4 , we did the Laue diffraction pattern (see Figure S2) and found the major feature of the Laue pattern is quite similar to the electron diffraction one.

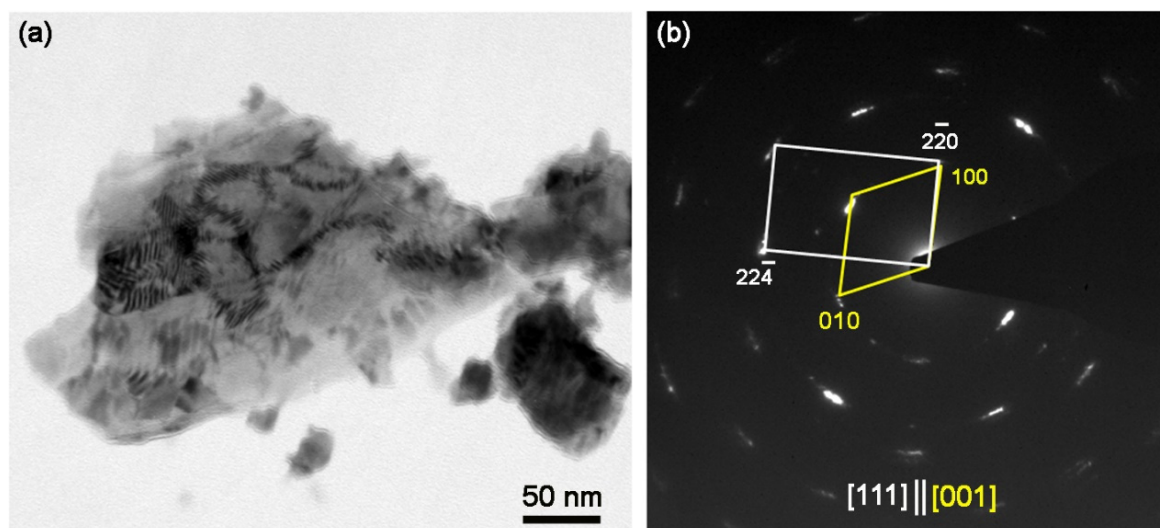


Figure 3. (a) TEM image of $(\text{CuCr}_2\text{Se}_4)_{0.4}(\text{CuCrSe}_2)_{0.6}$ sample. Clear Moiré fringes suggest that there is overlap of two phases. (b) Selected area electron diffraction pattern of $(\text{CuCr}_2\text{Se}_4)_{0.4}(\text{CuCrSe}_2)_{0.6}$ sample. Yellow lozenge shows the SAED pattern from the CuCrSe_2 phase, while white rectangle does from the CuCr_2Se_4 one. The orientation relationship between CuCrSe_2 and CuCr_2Se_4 is determined as $[001] (100) \parallel [111] (220)$. The broadening of reflection spots come from two phases and small misorientation of CuCrSe_2 layers.

The experimentally observed orientation-relationship between CuCrSe_2 and CuCr_2Se_4 can be easily understood by the atomic models of these two phases. Figure 4a,b are the

atomic structures of CuCr_2Se_4 projected along [111]-direction and CuCrSe_2 along [001]-one, respectively. To highlight the similarity between these two compounds, only Cr and Se atoms are drawn in this figure. One can see that Cr-Cr atoms in CuCrSe_2 form the triangle lattice, while those in CuCr_2Se_4 form a honeycomb-like one. The nearest Cr-Cr atomic distance in CuCrSe_2 is around 3.669 Å, which is quite close to that in CuCr_2Se_4 (3.655 Å), which suggests the semi-coherent interface between CuCr_2Se_4 and CuCrSe_2 . Therefore, we can observe the orientation relationship between CuCrSe_2 and CuCr_2Se_4 by TEM.

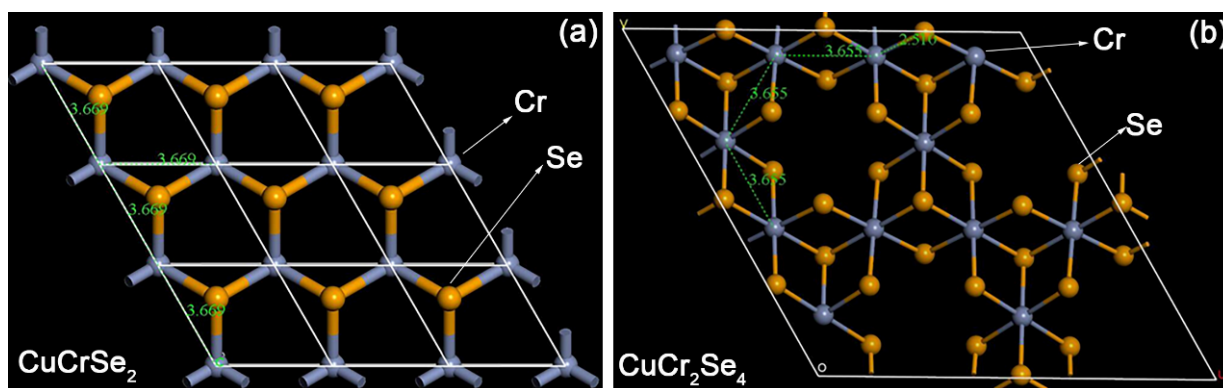


Figure 4. Atomic lattice structures of CuCrSe_2 (a) and CuCr_2Se_4 (b) projected along [001]- and [111]-direction, respectively. To highlight the similarity between these two compounds, only Cr and Se atoms are drawn in this figure. One can see that Cr-Cr atoms in CuCrSe_2 form the triangle lattice, while those in CuCr_2Se_4 forms a honeycomb-like one. The nearest Cr-Cr atomic distance in CuCrSe_2 is around 3.669 Å, which is quite close to that in CuCr_2Se_4 (3.655 Å), which suggests the semi-coherent interface between CuCr_2Se_4 and CuCrSe_2 .

Our TEM characterization suggests that CuCrSe_2 layers are mainly stacked with CuCr_2Se_4 along the c -axis of CuCrSe_2 or 111-axis of CuCr_2Se_4 . Therefore, we think the modified thermoconductivity mainly happens along the out-of-plane direction. The out-of-plane thermal conductivity (κ) of these CuCr_2Se_4 - CuCrSe_2 hetero-composite crystals was measured by TDTR from 60 to 300 K. Figure 5 summarizes the experimental and fitting of TDTR data of $(\text{CuCr}_2\text{Se}_4)_{1-x}(\text{CuCrSe}_2)_x$ measured at 300 K on how to extract their thermal conductivity. Inset of Figure 5 presents the $-V_{\text{in}}/V_{\text{out}}$ signals of one sample ($x = 0.8$) measured at room temperature and the associated fittings. Reasonable fitting exhibits the reliability of the measurements. On conducting the same experiment at different temperatures on three samples, the temperature-dependent out-of-plane thermal conductivities of $(\text{CuCr}_2\text{Se}_4)_{1-x}(\text{CuCrSe}_2)_x$ were obtained and are shown in Figure 5. Although TDTR measures thermal conductivities including both electron- and phonon-thermal conductivity, the electrical thermal conductivity (κ_e) is almost negligible, compared to κ_L . One can see from Figure 5 that at low temperature (from 60 to 180 K), the κ of these samples increases monotonously with temperature T raised, then κ in hetero-composite $(\text{CuCr}_2\text{Se}_4)_{1-x}(\text{CuCrSe}_2)_x$ ($x = 0.8, 0.6$) are nearly saturated when T is increased from 180 to 300 K; however, κ in $(\text{CuCr}_2\text{Se}_4)_{0.06}(\text{CuCrSe}_2)_{0.94}$ has a maximum value at about 200 K and then decreases when T is increased from 200 to 300 K.

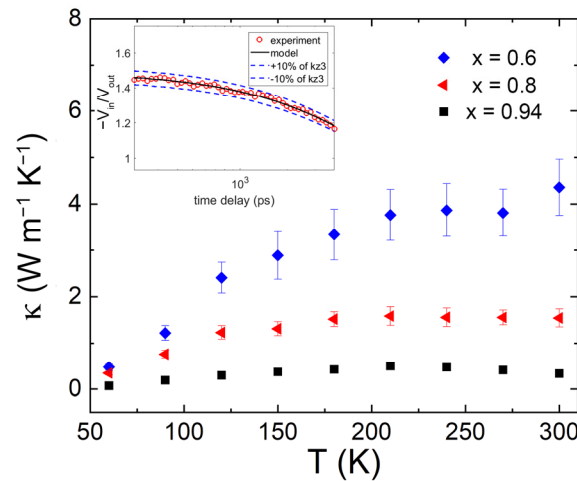


Figure 5. Temperature-dependent out-of-plane thermal conductivity of single $(\text{CuCr}_2\text{Se}_4)_{1-x}(\text{CuCrSe}_2)_x$ ($x = 0.94, 0.8, 0.6$) crystals measured by the TDTR method. Inset is $-V_{\text{in}}/V_{\text{out}}$ signal of $(\text{CuCr}_2\text{Se}_4)_{0.06}(\text{CuCrSe}_2)_{0.94}$ sample measured by the TDTR method at room temperature and fitted with a theoretical model to extract thermal conductivity.

To quantitatively understand the above-mentioned different κ - T behaviors, we fitted experimental κ_L data using the Debye-Callaway model [24,25]:

$$\kappa_L = \frac{k_B}{2\pi^2 v} \left(\frac{k_B}{\hbar} \right)^3 T^3 \int_0^{\theta_D/T} \frac{x^4 e^x}{\tau_c^{-1} (e^x - 1)} dx \quad (1)$$

where $x = \hbar\omega/k_B T$ is a dimensionless number, ω is the phonon frequency, k_B is the Boltzmann constant, \hbar is the reduced Planck constant, θ_D is the Debye temperature, v is the velocity of sound, and τ_c^{-1} is the phonon scattering relaxation time. The phonon relaxation rate can be written as:

$$\tau_c^{-1} = \frac{v}{L} + B\omega^2 T e^{-\theta_D/T} + C \frac{\left(\frac{\omega_0 \gamma}{2\pi^2} \right) \omega^2}{(\omega_0^2 - \omega^2)^2 + \left(\frac{\gamma}{\pi} \right)^2 \omega_0^2 \omega^2} \quad (2)$$

where L is the average size of lamellae leading to interface scattering, and B is a fitting parameter of three-phonon Umklapp scattering. The first, second, and third terms on the right side of Equation (2) represent interfacial scattering, three-phonon Umklapp scattering (anharmonic effect), and phonon resonance scattering, respectively. In the fitting process, we found that the C value in these compounds is too small, compared with that in previous literature [26,27]. The small C suggests the negligible effect of phonon resonance scattering in CuCrSe_2 at $T < 300$ K, which is different from the high-temperature case ($T > 365$ K) where phonon resonance scattering is crucial to κ of CuCrSe_2 , as reported previously [12]. Therefore, in what follows, we only report the fitting results based on the first two terms in Equation (2). The fitting results are shown in the solid curves of Figure 6a. The data of $(\text{CuCr}_2\text{Se}_4)_{0.06}(\text{CuCrSe}_2)_{0.94}$ are enlarged at the inset of Figure 6a because of its much smaller κ , compared to other samples. Evidently, experimental κ can be well fitted by Equation (1). The fitting parameters L and B are summarized in Table 1. As read from Table 1, with the increasing of the percentage of CuCrSe_2 , the L decreases monotonously, which indicates the increase of the interfacial-scattering contribution. As to the minimum L observed in CuCrSe_2 crystal, this is because the Cr and CuSe_2 layers are stacked alternatively along the c -axis. In this case, the small angle misorientation in CuCrSe_2 is quite universally observed (see electron diffraction in Figure 3b). These small-angle misorientated interfaces can lead to phonon scattering. While CuCr_2Se_4 is a cubic crystal, the misorientation is difficult to observe. Therefore, if the concentration of CuCrSe_2 is higher, L is decreased because there is high density of small-angle misorientation grains. As far as three-phonon

scattering is concerned, in $(\text{CuCr}_2\text{Se}_4)_{0.4}(\text{CuCrSe}_2)_{0.6}$ and $(\text{CuCr}_2\text{Se}_4)_{0.2}(\text{CuCrSe}_2)_{0.8}$ crystal, the fitting parameter B is changed from about 1×10^{-18} – 1×10^{-17} s/K. However, the fitting parameter B in $(\text{CuCr}_2\text{Se}_4)_{0.06}(\text{CuCrSe}_2)_{0.94}$ is 4×10^{-16} s/K, which is 25 times larger than that of $(\text{CuCr}_2\text{Se}_4)_{0.4}(\text{CuCrSe}_2)_{0.6}$. This suggests that there is more significant umklapp scattering in $(\text{CuCr}_2\text{Se}_4)_{0.06}(\text{CuCrSe}_2)_{0.94}$ than in the other two samples.

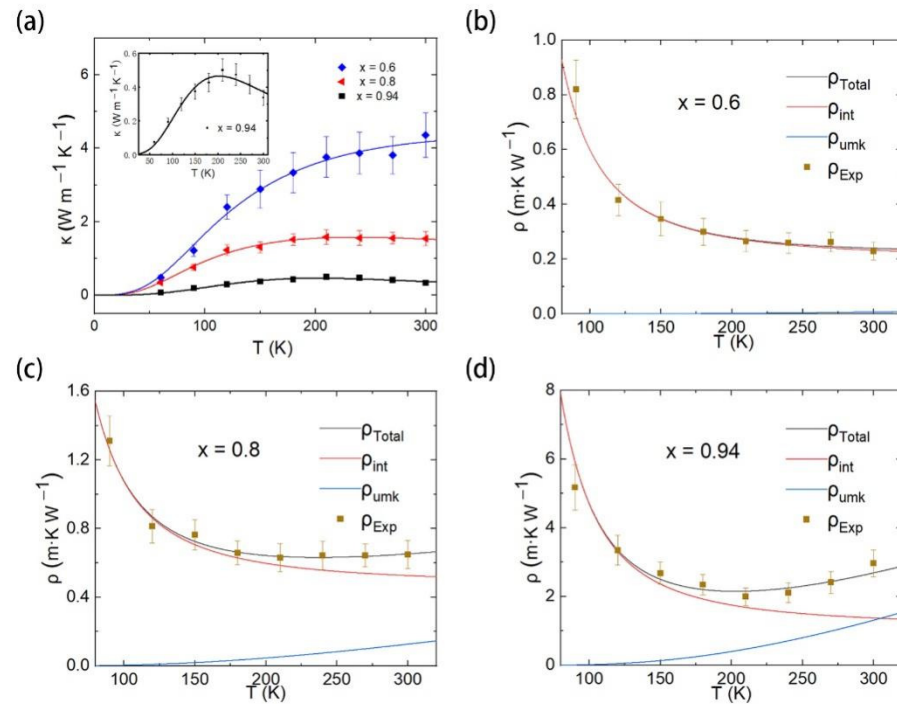


Figure 6. (a) Fittings of experimental thermoconductivities of single $(\text{CuCr}_2\text{Se}_4)_{1-x}(\text{CuCrSe}_2)_x$ ($x = 0.94, 0.8, 0.6$) crystals by the Debye–Callaway model. Inset is the enlarged data of $(\text{CuCr}_2\text{Se}_4)_{0.06}(\text{CuCrSe}_2)_{0.94}$. (b–d) Relative contribution of three-phonon Umklapp scattering and interfacial scattering to thermal resistivity in $(\text{CuCr}_2\text{Se}_4)_{1-x}(\text{CuCrSe}_2)_x$ ($x = 0.94, 0.8, 0.6$).

Table 1. The parameters in fitting thermal conductivity of samples by the Debye–Callaway model.

	L (nm)	B (s/K)	θ_D (K)
$(\text{CuCr}_2\text{Se}_4)_{0.4}(\text{CuCrSe}_2)_{0.6}$	0.58	1.12×10^{-18}	529
$(\text{CuCr}_2\text{Se}_4)_{0.2}(\text{CuCrSe}_2)_{0.8}$	0.42	1.33×10^{-17}	444
$(\text{CuCr}_2\text{Se}_4)_{0.06}(\text{CuCrSe}_2)_{0.94}$	0.36	3.75×10^{-16}	430

To more quantitatively determine the contribution of interface scattering and Umklapp scattering in CuCr_2Se_4 – CuCrSe_2 hetero-composites, we analyzed thermal resistivity ρ ($\rho = 1/\kappa_L$), rather than thermal conductivity κ . According to the Matthiessen rule, the ρ is the summation of thermal resistivity coming for the interface and three-phonon Umklapp scattering (according to the above discuss, the resonance scattering is negligible). Mathematically:

$$\rho_{total} = \rho_{umk} + \rho_{int} \quad (3)$$

where $\rho_{total} = 1/\kappa_L$, $\rho_{int} = 1/\kappa_{int}$, and the thermal conductivity of interfacial scattering is:

$$\kappa_{int} = \frac{k_B}{2\pi^2v} \left(\frac{k_B}{\hbar} \right)^3 T^3 \int_0^{\theta_D/T} \frac{x^4 e^x}{L(e^x - 1)} dx \quad (4)$$

Combining Equations (3) and (4), we can determine the thermal resistivity coming from interface scattering and three-phonon Umklapp scattering (see Figure 6b–d). One can see from Figure 6b–d that in $(\text{CuCr}_2\text{Se}_4)_{0.4}(\text{CuCrSe}_2)_{0.6}$ interface scattering nearly contributes all

thermal resistivity, and in $(\text{CuCr}_2\text{Se}_4)_{0.2}(\text{CuCrSe}_2)_{0.8}$ the interface scattering and Umklapp scattering roughly contribute 80% and 20% thermal resistivity, respectively. Different forms of these two samples, Umklapp scattering in $(\text{CuCr}_2\text{Se}_4)_{0.06}(\text{CuCrSe}_2)_{0.94}$ is more significant to thermal resistivity at, for example, 300 K, where the contribution of umklapp scattering is larger than interface scattering. In other words, in $(\text{CuCr}_2\text{Se}_4)_{0.06}(\text{CuCrSe}_2)_{0.94}$, both interface scattering and Umklapp scattering lead to the lowest thermal conductivity therein.

4. Conclusions

In this work, taking advantage of CuCr_2Se_4 being easily precipitated from CuCrSe_2 matrix, we grew a series of hetero-composite CuCrSe_2 - CuCr_2Se_4 crystals by adjusting the growth conditions. The orientation relationship between CuCrSe_2 and CuCr_2Se_4 is $[001] (100) \parallel [111] (220)$ determined by electron diffraction. The out-of-plane thermal conductivity κ of these crystals was measured by using the time-domain thermoreflectance (TDTR) method. Analysis of thermal resistivity of these hetero-composites, by Boltzmann-Callaway models, suggests that interface scattering plays a quite significant role to κ in $(\text{CuCr}_2\text{Se}_4)_{0.4}(\text{CuCrSe}_2)_{0.6}$ and $(\text{CuCr}_2\text{Se}_4)_{0.2}(\text{CuCrSe}_2)_{0.8}$ hetero-composites, but it is both anharmonic three-phonon and interface scattering leading to the lowest thermal conductivity in $(\text{CuCr}_2\text{Se}_4)_{0.06}(\text{CuCrSe}_2)_{0.94}$. Our results reveal the thermal conductivity evolution in CuCr_2Se_4 - CuCrSe_2 hetero-composites.

Supplementary Materials: The following supporting information can be downloaded at: <https://www.mdpi.com/article/10.3390/cryst12030433/s1>, Figure S1: XRD pattern of synthesized CuCrSe_2 polycrystalline powder. Figure S2: (a) The Laue pattern of composite of CuCrSe_2 and CuCr_2Se_4 . The red rectangles highlight the broadening and splitting reflection spots that consist of the reflection spots of CuCrSe_2 and CuCr_2Se_4 , compared with electron diffraction (two red rectangle) shown in (b). Based on this comparison, though the resolution of Laue pattern is poor, the orientation relationship between CuCrSe_2 and CuCr_2Se_4 determined through electron diffraction is correct.

Author Contributions: H.L.: investigation, data curation and writing—original draft. C.Y.: formal analysis and writing—original draft. R.Z.: investigation and writing—review and editing. Y.Z.: investigation. Y.L.: investigation and formal analysis. M.L.: supervision. J.Z.: software. S.Y.: conceptualization and methodology. Y.C.: methodology. All authors have read and agreed to the published version of the manuscript.

Funding: We'd like to acknowledge the financial support from the National Natural Science Foundation of China (51872134, 51902152, 51890861 and 11890702), the Foundation for Innovative Research Groups of the National Natural Science Foundation of China (51721001), and the National Key R&D Program of China (2016YFA0201104). Yang-Yang Lv acknowledges financial support from the Innovation Program for the Talents of China Postdoctoral Science Foundation (BX20180137) and support from the China Postdoctoral Science Foundation (2019M650105).

Institutional Review Board Statement: Not applicable.

Informed Consent Statement: Not applicable.

Data Availability Statement: Not applicable.

Conflicts of Interest: The authors declare no conflict of interest and declare that they have no known competing financial interests or personal relationships that could have appeared to influence the work reported in this paper.

References

1. Singh, K.; Maignan, A.; Martin, C.; Simon, C. AgCrS_2 : A Spin Driven Ferroelectric. *Chem. Mater.* **2009**, *21*, 5007–5009. [[CrossRef](#)]
2. Yang, H.; Huang, Z.; Jia, T.; Zhang, X.; Zeng, Z. Magnetic ordering and exchange striction stabilized geometric ferroelectricity in multiferroic AgCrS_2 . *J. Physics Condens. Matter* **2016**, *28*, 236002. [[CrossRef](#)]
3. Damay, F.; Petit, S.; Braendlein, M.; Rols, S.; Ollivier, J.; Martin, C.; Maignan, A. Spin dynamics in the unconventional multiferroic AgCrS_2 . *Phys. Rev. B* **2013**, *87*, 134413. [[CrossRef](#)]
4. Damay, F.; Martin, C.; Hardy, V.; André, G.; Petit, S.; Maignan, A. Magnetoelastic coupling and unconventional magnetic ordering in the multiferroic triangular lattice AgCrS_2 . *Phys. Rev. B* **2011**, *83*, 184413. [[CrossRef](#)]

5. Apostolova, I.N.; Apostolov, A.T.; Wesselinowa, J.M. Differences in the multiferroic properties of AgCrS₂ and AgCrO₂. *Solid State Commun.* **2021**, *323*, 114119. [[CrossRef](#)]
6. Kanematsu, T.; Okamoto, Y.; Takenaka, K. Large magnetic-field-induced strain at the magnetic order transition in triangular antiferromagnet AgCrS₂. *Appl. Phys. Lett.* **2021**, *118*, 142404. [[CrossRef](#)]
7. Yan, Y.; Guo, L.; Zhang, Z.; Lu, X.; Peng, K.; Yao, W.; Dai, J.; Wang, G.; Zhou, X. Sintering temperature dependence of thermoelectric performance in CuCrSe₂ prepared via mechanical alloying. *Scr. Mater.* **2017**, *127*, 127–131. [[CrossRef](#)]
8. Bhattacharya, S.; Basu, R.; Bhatt, R.; Pitale, S.; Singh, A.; Aswal, D.K.; Gupta, S.K.; Navaneethan, M.; Hayakawa, Y. CuCrSe₂: A high performance phonon glass and electron crystal thermoelectric material. *J. Mater. Chem. A* **2013**, *1*, 11289–11294. [[CrossRef](#)]
9. Tewari, G.C.; Tripathi, T.; Yamauchi, H.; Karppinen, M. Thermoelectric properties of layered antiferromagnetic CuCrSe₂. *Mater. Chem. Phys.* **2014**, *145*, 156–161. [[CrossRef](#)]
10. Niedziela, J.L.; Bansal, D.; May, A.F.; Ding, J.; Lanigan-Atkins, T.; Ehlers, G.; Abernathy, D.L.; Said, A.; Delaire, O. Selective breakdown of phonon quasiparticles across superionic transition in CuCrSe₂. *Nat. Phys.* **2019**, *15*, 73–78. [[CrossRef](#)]
11. Li, B.; Wang, H.; Kawakita, Y.; Zhang, Q.; Feyngenson, M.; Yu, H.L.; Wu, D.; Ohara, K.; Kikuchi, T.; Shibata, K.; et al. Liquid-like thermal conduction in intercalated layered crystalline solids. *Nat. Mater.* **2018**, *17*, 226–230. [[CrossRef](#)] [[PubMed](#)]
12. Ding, J.; Niedziela, J.L.; Bansal, D.; Wang, J.; He, X.; May, A.F.; Ehlers, G.; Abernathy, D.L.; Said, A.; Alatas, A.; et al. Anharmonic lattice dynamics and superionic transition in AgCrSe₂. *Proc. Natl. Acad. Sci. USA* **2020**, *117*, 3930–3937. [[CrossRef](#)] [[PubMed](#)]
13. Gagor, A.; Gnida, D.; Pietraszko, A. Order–disorder phenomena in layered CuCrSe₂ crystals. *Mater. Chem. Phys.* **2014**, *146*, 283–288. [[CrossRef](#)]
14. Cheng, Y.; Yang, J.; Jiang, Q.; Fu, L.; Xiao, Y.; Luo, Y.; Zhang, D.; Zhang, M. CuCrSe₂ Ternary Chromium Chalcogenide: Facile Fabrication, Doping and Thermoelectric Properties. *J. Am. Ceram. Soc.* **2015**, *98*, 3975–3980. [[CrossRef](#)]
15. Abramova, G.; Pankrats, A.; Petrakovskii, G.; Rasch, J.C.E.; Boehm, M.; Vorotyntov, A.; Tugarinov, V.; Szumczak, R.; Bovina, A.; Vasilev, V. Electron spin resonance in CuCrSe₂ chromecopper disulphides synthesized by different methods. *J. Appl. Phys.* **2010**, *107*, 093914. [[CrossRef](#)]
16. Han, H.; Zhang, L.; Tong, W.; Qu, Z.; Zhang, C.; Pi, L.; Zhang, Y. The in-plane ferromagnetic ordering in half-metallic CuCr₂Se₄-xBr_x (x = 0.25) single crystal. *J. Alloys Compd.* **2016**, *685*, 304–308. [[CrossRef](#)]
17. Yogi, A.; Bera, A.K.; Maurya, A.; Kulkarni, R.; Yusuf, S.M.; Hoser, A.; Tsirlin, A.A.; Thamizhavel, A. Stripe order on the spin-1 stacked honeycomb lattice in Ba₂Ni(PO₄)₂. *Phys. Rev. B* **2017**, *95*, 024401. [[CrossRef](#)]
18. Yano, R.; Sasagawa, T. Crystal Growth and Intrinsic Properties of ACrX₂ (A = Cu, Ag; X = S, Se) without a Secondary Phase. *Cryst. Growth Des.* **2016**, *16*, 5618–5623. [[CrossRef](#)]
19. Cao, L.; Pan, J.; Zhang, H.; Zhang, Y.; Wu, Y.; Lv, Y.-Y.; Yan, X.-J.; Zhou, J.; Chen, Y.B.; Yao, S.-H.; et al. One-Order Decreased Lattice Thermal Conductivity of SnSe Crystals by the Introduction of Nanometer SnSe₂ Secondary Phase. *J. Phys. Chem. C* **2019**, *123*, 27666–27671. [[CrossRef](#)]
20. Liu, D.; Dreßler, C.; Seyring, M.; Teichert, S.; Rettenmayr, M. Reduced thermal conductivity of Bi-In-Te thermoelectric alloys in a eutectic lamellar structure. *J. Alloy. Compd.* **2018**, *748*, 730–736. [[CrossRef](#)]
21. Kang, K.; Koh, Y.K.; Chiritescu, C.; Zheng, X.; Cahill, D.G. Two-tint pump-probe measurements using a femtosecond laser oscillator and sharp-edged optical filters. *Rev. Sci. Instrum.* **2008**, *79*, 114901. [[CrossRef](#)] [[PubMed](#)]
22. Cahill, D.G. Analysis of heat flow in layered structures for time-domain thermoreflectance. *Rev. Sci. Instrum.* **2004**, *75*, 5119–5122. [[CrossRef](#)]
23. Yan, X.-J.; Lv, Y.-Y.; Li, L.; Li, X.; Yao, S.-H.; Chen, Y.-B.; Liu, X.-P.; Lu, H.; Lu, M.-H.; Chen, Y.-F. Investigation on the phase-transition-induced hysteresis in the thermal transport along the c-axis of MoTe₂. *NPJ Quantum Mater.* **2017**, *2*, 31. [[CrossRef](#)]
24. Callaway, J. Model for Lattice Thermal Conductivity at Low Temperatures. *Phys. Rev. (Series I)* **1959**, *113*, 1046–1051. [[CrossRef](#)]
25. Callaway, J.; von Baeyer, H.C. Effect of point imperfections on lattice thermal conductivity. *Phys. Rev.* **1960**, *120*, 1149. [[CrossRef](#)]
26. Di, C.; Yu, Y.-S.; Luo, Y.-C.; Lin, D.-J.; Yan, X.-J.; Lu, M.-H.; Zhou, J.; Yao, S.-H.; Chen, Y.B. Ultralow Lattice Thermal Conductivity of A_{0.5}RhO₂ (A = K, Rb, Cs) Induced by Interfacial Scattering and Resonant Scattering. *J. Phys. Chem. C* **2021**, *125*, 11648–11655. [[CrossRef](#)]
27. Yang, J.; Morelli, D.T.; Meisner, G.P.; Chen, W.; Dyck, J.S.; Uher, C. Effect of Sn substituting for Sb on the low-temperature transport properties of ytterbium-filled skutterudites. *Phys. Rev. B* **2003**, *67*, 165207. [[CrossRef](#)]